Delft University of Technology

Methods to actively modify the dynamic response of cm-scale FWMAV designs

Peters, H. J.; Goosen, J. F L; van Keulen, A.

Important note
To cite this publication, please use the final published version (if applicable).
Please check the document version above.

Methods to Actively Modify the Dynamic Response of cm-Scale FWMAV Designs

H.J. Peters[1,2], J.F.L. Goosen[1] and F. van Keulen[1]

[1]Structural Optimization & Mechanics, Department of Precision and Microsystems Engineering, Faculty of Mechanical, Maritime and Material Engineering, Delft University of Technology, Mekelweg 2, 2628 CD Delft, The Netherlands
[2]DevLab, Development Laboratories, Horsten 1, MMP 0.10, 5612 AX Eindhoven, The Netherlands

E-mail: `h.j.peters-1@tudelft.nl`, `j.f.l.goosen@tudelft.nl`, `a.vankeulen@tudelft.nl`

Abstract. Lightweight vibrating structures (such as Flapping Wing Micro Air Vehicle (FWMAV) designs) often require some form of control. To achieve controllability, local structural property changes (e.g., damping and stiffness changes) might be induced in an active manner. The stroke-averaged lift force production of a FWMAV wing can be modified by changing the structural properties of that wing at carefully selected places (e.g., changing the properties of the elastic hinge at the wing root as studied in this work). To actively change the structural properties, we investigate three different methods which are based on: 1) piezoelectric polymers, 2) electrorheological fluids, and 3) electrostatic softening. This work aims to gain simple yet insightful ways to determine the potential of these methods without focusing on the precise modeling. Analytical models of FWMAV wing designs that include control approaches based on these three methods are used to calculate the achievable lift force modifications after activating these methods. The lift force production as a result of a wing flapping motion is determined using a quasi-steady aerodynamic model. Both piezoelectric polymers and electrostatic softening are found to be promising in changing the structural properties and, hence, the lift force production of FWMAV wings. For the control of lightweight FWMAV designs, numerical simulations reveal a promising roll maneuverability due to the induced lift force difference between a pair of opposite wings. Although applied to a specific FWMAV design, this work is relevant for control of small, lightweight, possible compliant, vibrating structures in general.

1. Introduction

The control of small, lightweight, possibly compliant vibrating structures is often complicated by constraints on, for example, weight and power consumption. Control is, however, required in many practical situations. For example, to attenuate undesired dynamic responses [1], to tune the resonance frequency of energy harvesters to maximize the electric power output [2], or to ensure the desired functioning of complex flying structures [3]. To tackle these various structural control challenges, research on control approaches is still very active (see, for example, [4]).

One specific class of lightweight, potentially compliant, complex vibrating structures are Flapping Wing Micro Air Vehicles (FWMAV). Potential applications of FWMAV designs are in, among others, surveillance (e.g., police), information gathering (e.g., events monitoring), and in the inspection of inaccessible areas. FWMAV designs are dynamically excited to induce a repetitive flapping of the wings in order to generate the required lift to stay aloft. FWMAVs require active control for stable flight, hovering, and maneuvering which is even more necessary due to the intrinsic instability of these designs. The control of FWMAV designs is complicated by constraints on weight, power consumption, space limitations, and robustness. Additionally, the control mechanism often needs to allow for large deformations, rotations and translations.

The dynamic response due to a harmonic excitation can be approximated by the eigensolutions (i.e., eigenmodes and eigenfrequencies) of the structural design [5]. These eigensolutions are determined by the structural properties (i.e., mass, damping, stiffness and their spatial distribution) of the design. Hence, carefully selected and actively induced (local) structural property changes can be used to modify the eigensolutions and, consequently, the dynamic response in a desired way. Methods to actively induce these property changes are, for example, adjusting the electric circuit of piezoelectric patches [6], changing the effective viscosity of smart fluids [7], inducing geometrical changes such as curvature [8], and temperature stimuli of shape memory materials [9].

Despite all research on methods to induce property changes, the integration of these methods within designs with, for example, stringent weight constraints (e.g., FWMAV designs), is not well established in literature. This work aims, consequently, to integrate methods for inducing structural property changes into a FWMAV design to enable active control of the dynamic flap response. The application requires the control method to be lightweight, integrable, power efficient, and robust. Although presented for a very specific FWMAV design, these control methods are equably applicable on other complex, compliant structural dynamic applications with comparable constraints.

This work considers active methods for the control of a four wing FWMAV design as shown in figure 1. The design uses a ring-type transmission mechanism to convert the linear actuator motion into a repetitive flapping motion of the four wings in the horizontal plane [10]. The $0.5cm$ wingspan, flapping frequency, and mass of this FWMAV design is 12 cm, 27 Hz, and 4 gram, respectively.

To reduce actuation and design complexity, an elastic hinge is integrated into the wing design enabling the wing pitching motion to be passive during the driven flapping motion. The wing pitching angle has to vary along with the flapping motion and is crucial for a correct determination of the aerodynamic performance. Due to the inertial and aerodynamic loading during the flapping motion, a properly tuned elastic hinge enables the required pitching motion to achieve enough lift to stay aloft. The effective rotational stiffness of the elastic hinge, which is primarily loaded in bending, can be given by [11]:

$$k_{\rm rot} = \frac{EI}{L}, \tag{1}$$

where E, I, and L are the Young's modulus, the second moment of area, and the length of the elastic hinge, respectively.

In this work, the elastic hinge is replaced by an active hinge design for which the structural properties (i.e., damping and stiffness) can be changed due to external stimuli (e.g., an electric field). The passive pitching motion and, hence, the stroke-averaged lift force will change if the structural properties of the active hinge are adjusted, thus, enabling maneuvering. Changing the structural properties of the active hinge is complicated by the small scale, the required large deflection during pitching, the desired robustness, and the necessary low weight. These complications require an elegant and integrable solution.
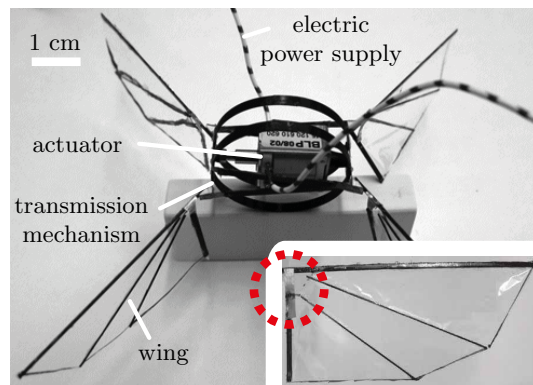

Figure 1. Four wing FWMAV design with a frontal view of the wing design with the encircled elastic (spring steel) hinge.

This paper is organized as follows. Section 2 describes the working principle of three methods to induce structural property changes within the context of lightweight FWMAV structures. In section 3 these methods are integrated into an analytical passive pitching wing model to quantitatively determine the effectiveness in controlling the wing performance (i.e., lift force without quantifying power consumption yet). Section 4 studies numerically the FWMAV roll-maneuverability due to the actively induced lift force differences between a pair of opposite wings. The consequences and limitations of the obtained results are discussed in section 5. Section 6 presents conclusions and recommendations for further research.

2. Methods to induce structural property changes

There are numerous methods to induce (local) structural property changes and attempts have been made to categorize them [12, 13]. In a previous study [13] a qualitative comparison was done to select methods that are most applicable to be integrated in compliant FWMAV designs with stringent weight constraints. That inventory resulted in four promising candidates for a lightweight, integrable, power efficient and robust control method: i) interaction of stacked layers, ii) piezoelectric polymers, iii) smart fluids (e.g., electrorheological fluids), and iv) electrostatic softening. On the other hand, methods driven by temperature stimuli are rejected due to their low power efficiency and limited response time as determined by the relatively long cooling time. In addition, methods that only allow small deflections and rotations to maintain structural stability are less applicable in a FWMAV context. Methods that require additional support-structures (e.g., linkages) to function properly are also discarded since these support-structures add mass and complexity to the system while decreasing reliability.

The functioning of the first promising method (i.e., interaction of stacked layers) has been recently demonstrated both analytically and experimentally [14]. With this method, the bending stiffness of an elastic hinge consisting of stacked layers is changed by modifying the interaction between these layers (i.e., the layers stick or slip with respect to each other). Electrostatics is used to stick together the conducting layers which are separated by a dielectric foil. Experiments showed significant modifications of the dynamic response. Practical implementation of this method within FWMAVs requires: i) endurance tests to study the influence of wear on the performance and ii) practical tools to accurately produce the stacked layers consisting of very thin layers (i.e., $\leq 20\,\mu$m).

In the remainder of this section, the working principle of the remaining three promising methods is given (i.e., piezoelectric polymers, electrorheological fluids and electrostatic softening). This work does not aim to precisely model the functioning of the different methods but rather gain simple yet insightful ways to determine whether or not a method is applicable for the control of structures with stringent weight and power constraints.

2.1. Piezoelectric polymers

Much research has been done to integrate piezoelectric materials in lightweight dynamic structures. Piezoelectric materials may serve as a sensor (i.e., producing an electric charge on the surface of the material if mechanically strained, the *direct piezoelectric effect*), or as an actuator (i.e., inducing mechanical strain if the material is placed inside an electric field, the *converse piezoelectric effect*). Due to the large FWMAV wing hinge deflections, the compliant piezoelectric polymers (e.g., PVDF) are more appealing as compared to the stiff and brittle piezoelectric ceramics (e.g., PZT). Generally, piezoelectric ceramics outperform piezoelectric polymers for actuation [15].

Piezoelectric materials can induce effective (local) structural property changes in different ways. For example, by *active control approaches* that require actuators, sensors and external power supplies [1], by *passive control approaches* that use shunted electrical networks (e.g., with a resistor and/or inductor) [16], or by *state-switching approaches* that use switches to switch between different piezoelectric material properties corresponding to open or closed electric circuits [6]. The effectiveness of the different approaches to induce property changes depends on, among others, a careful tuning of the electric network and an accurate positioning of piezoelectric material within the structure.

For FWMAV applications, an approach similar to state-switching is appealing due to the intrinsic simplicity of controlling just a switch. Disadvantages of the active control approaches are the required high control voltages and the additional sensors while the passive control approaches induce only constant (i.e., not controllable) property changes which makes them not very useful for active response modifications. The initially defined state-switching approach [6], switches at four accurately defined times during a full cycle of motion (i.e., after every quarter cycle). For practical implementation of this control approach, an additional observer scheme needs to be utilized to accurately determine these switching times [17].

Alternatively, a simple, single opening or closing of the switch with the corresponding steady-state difference of the piezoelectric material properties might
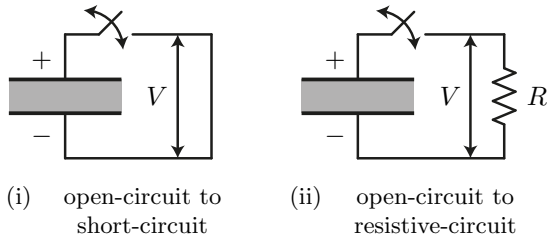
(i) open-circuit to short-circuit
(ii) open-circuit to resistive-circuit

Figure 2. Schematics of the two utilized switch circuits with a voltage V over the piezoelectric material.

be sufficient for control. This means utilizing the steady-state piezoelectric material property difference corresponding to different electric circuits rather than switching frequently between the different circuits. The switch circuits of interest are, see figure 2:

(i) switch from open-circuit (OC) to short-circuit (SC), and

(ii) switch from open-circuit (OC) to resistive-circuit (RC) (i.e., R-shunt).

Another well-known circuit which might induce significant property changes (i.e., damping) is the resistive-inductor-circuit (i.e., RL-shunt) [18]. This circuit, however, requires a high inductance value in order to function properly (especially for the relatively low frequencies of interest in this study). It is practically impossible to manufacture such inductors within the space and weight constraints of the FWMAV design.

By switching between different electrical boundary conditions, the electromechanical coupling factor plays an important role. This factor is operational-mode dependent and measures the conversion effectiveness of mechanical energy into electrical energy and *visa versa*. For a mechanical force in j-direction (where $j = 1, \ldots, 6$ representing the three orthogonal and three shear directions) and an electric field in i-direction (where $i = 1, 2, 3$ representing three orthogonal directions), this factor is, corresponding to standard piezoelectric material conventions, given by [16]

$$k_{ij} = \frac{d_{ij}}{\sqrt{s_{jj}^{\mathrm{E}}\varepsilon_i^{\mathrm{T}}}}. \qquad (2)$$

In (2), d_{ij} represents the piezoelectric material coupling constant, s_{jj} represents the piezoelectric compliance, ε_i represents the piezoelectric dielectric permittivity constant, and the superscripts E and T indicate that the parameter was measured at constant electric field or stress, respectively. Generally, k_{ij} is more significant for piezoelectric ceramics compared to piezoelectric polymers (i.e., approximately 0.7 vs 0.1 [1]).

By switching from OC to SC (i.e., figure 2 (i)), the compliance of the piezoelectric material changes

without introducing any damping. The relation between the OC compliance and the SC compliance can be given by [16]

$$s_{jj}^{\mathrm{OC}} = s_{jj}^{\mathrm{SC}}\left(1 - k_{ij}^2\right), \qquad (3)$$

resulting in a higher compliance (i.e., lower stiffness) for the SC piezoelectric material. The compliance corresponding to a constant electric field, s_{jj}^{E}, is equal to the SC compliance, s_{jj}^{SC}. (3) shows that the difference in compliance between the OC and SC configuration is directly related to the electromechanical coupling k_{ij}.

Switching from OC to RC (i.e., figure 2 (ii)) results in: 1) energy dissipation through the resistor and 2) a higher compliance. The increase in compliance is, however, less compared to the change found in circuit (i) since the OC and SC configurations provide the compliance extrema [6]. The non-dimensional damping ratio ζ (i.e., if $\zeta > 1$ the system is over-damped) can be maximized at the frequency of interest (i.e., the flapping frequency), by a proper tuning of the resistor value according to the given capacitance of the piezoelectric material. The maximum attainable damping ratio can be approximated by [18]

$$\zeta^{\mathrm{max}} = \frac{k_{ij}^2}{4\left(1 - k_{ij}^2\right)}, \qquad (4)$$

which shows an increase of the property change (i.e., an increase of damping) if the electromechanical coupling factor k_{ij} increases. Because of the large deformations, the application of piezoelectric material in the FWMAV wing hinge is restricted to piezoelectric polymers for which the electromechanical coupling factor is relatively moderate. This reduces the potential achievable structural property change.

2.2. Embedded smart fluid

A smart fluid (i.e., magnetorheological fluid (MRF) [19] or electrorheological fluid (ERF) [20]) transforms rapidly (i.e., milliseconds) into a weak viscoelastic solid upon exposure to an external magnetic or electric field since the constituent particles form chains in the direction of the induced field lines as shown schematically in figure 3 [21]. This chain formation, effectively, alters the maximal yield stress of the fluid. Whenever mechanically loaded below the yield stress, the fluid behaves as a viscoelastic solid and beyond the yield stress it behaves like a fluid. The maximal field-induced yield stress depends on the fluid composition (e.g., particle volume fraction) and is, generally, higher for MRF as compared to ERF [22]. This initial feasibility study neglects the influence of the ER-fluid particle size on the mechanical performance.

To actively modify smart fluid properties, the external magnetic or electric field needs to be
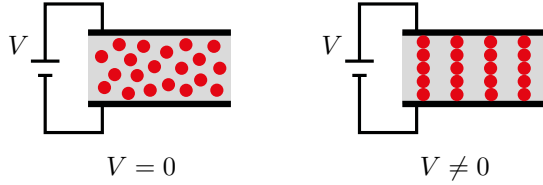
Figure 3. Schematic of the chain formation of constituent particles (i.e., red spheres) in an ERF between conducting plates due to an external field as induced by the potential voltage V.

controlled. Electromagnets or movable permanent magnets can be applied to control the magnetic field for MRF whereas, relatively simple, electrostatics can be used to change the electric field in the case of ERF. For use in FWMAV designs with stringent weight constraints, a controllable magnetic field with sufficient range becomes rather cumbersome and is, consequently, infeasible. As such, the use of smart fluids to induce structural property changes within FWMAV designs is restricted to ERFs.

The behavior of ERFs (and smart fluids in general) as a function of the electric field is modeled using both viscoelastic and viscoplastic models. The *viscoelastic models* can be classified according to their solid-like or fluid-like behavior [23] and are specified in the frequency domain using a complex modulus G^* (i.e., $G^* = G' + iG''$, where G' represents the elastic or storage modulus, and G'' indicates the viscous or loss modulus). Subsequently, for a given harmonic shear strain γ (i.e., $\gamma = \gamma_0 \sin(\omega t)$, where γ_0, ω and t represent the shear strain amplitude, the frequency, and the time, respectively), the shear stress τ is given by [24]

$$\tau = G'\gamma_0 \sin(\omega t) + G''\gamma_0 \cos(\omega t), \tag{5}$$

where both G' and G'' depend on the applied field. Viscoelastic models are often used to study the effect of ERF-based constrained layer dampers to attenuate structural vibrations [25]. *Viscoplastic models*, on the other hand, model the fluid behavior in the time-domain. The Bingham plastic (BP) model, which describes the fluid as an elastic solid at low stresses (i.e., pre-yield) and as a viscous fluid at higher stresses (i.e., post-yield), is the most common viscoplastic model. The shear stress vs shear strain rate relation for the BP model is given by [26]

$$\tau = \tau_y + \mu\dot{\gamma}, \tag{6}$$

where τ_y represents the field dependent yield stress, μ the field dependent viscosity, and $\dot{\gamma}$ the shear strain rate. Viscoplastic models are, for example, often used to study the effect of ERF-based valves [27].

To determine the potential structural property changes that can be induced by the ERF, the model parameters as a function of the electric field (e.g., $G'(E)$, $G''(E)$, and $\tau_y(E)$) need to be known. The differences in experimental setup (e.g., shear strains and frequencies) and fluid composition (e.g., particle size and particle volume fraction) complicate the comparison between the different experimental studies [28, 29, 30]. Experimental results are generally obtained at larger scales as compared to the mm-scale configurations we aim for in this work. To apply the required electric field (i.e., approximately $5\,\text{kV/mm}$), high voltage power supplies are needed.

To improve the performance of a device that contains smart fluids an approach that combines a sophisticated or smart structural design *with* a smart fluid might be more effective to enhance, for example, shear strain rates or electric field strengths. A good example of this approach is a tunable stiffness element that uses surface micropatterning to spatially align domains of smart fluid to enhance interfacial sliding resistance [31].

Potential disadvantages of using ERF in FWMAV designs are: 1) sedimentation or clustering of the constituent particles over time leading to performance fluctuations, 2) the required sealing to prevent leakage, and 3) the lack of appropriate material compositions for mm-scale applications. The disadvantage of sedimentation can be solved by using electrorheological liquid crystals (LCs) which do not contain suspended particles. These LCs are applied in microsystems to build micro-valves [32].

2.3. Electrostatic softening

For decreasing dimensions, electrostatic loads start to prevail over other kinds of actuation (e.g., electromagnetics) [33]. Microelectromechanical systems (MEMS) use electrostatics to modify structural stiffness to tune, for example, resonance frequencies [34, 35]. The electrostatic force is inversely quadratic to the gap between the electrodes which limits the relative displacement between the electrodes.

Consider a simplified capacitor system with two parallel, rigid, infinite, perfectly conducting plates between which a voltage V is applied. The upper plate can move and is held by a spring with stiffness k per unit area while the lower plate is fixed. Newton's second law for this simplified capacitor system is, while neglecting gravity, given by

$$m\ddot{d} = -k(d - d_0) - \frac{1}{2}\varepsilon\frac{V^2}{d^2}, \tag{7}$$

where m is the mass per unit area of the plate, d represents the distance between the plates, d_0 is the distance between the plates when the spring is unstretched, and ε represents the uniform permittivity of the medium between the electrodes. By taking the
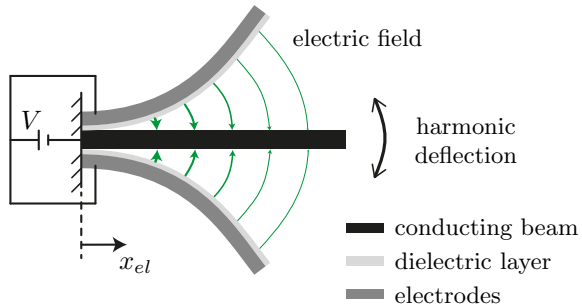
Figure 4. Harmonically deflecting, conducting beam between curved electrodes for which the effective bending stiffness decreases if the electric field increases.

derivative of (7) with respect to the displacement for an equilibrium position d_e, the total static structural stiffness (i.e., $m\ddot{d} = 0$) of this coupled problem is given by

$$-\left.\frac{\partial F}{\partial d}\right|_{d=d_e} = k - \varepsilon\frac{V^2}{d_e^3}, \tag{8}$$

where a minus sign is added since the stiffness is the variation of the internal static loads, F. The electric load (i.e., $-\varepsilon V^2/d_e^3$) introduces negative stiffness to the system. The total stiffness is equal to zero at the so-called *pull-in voltage* after which the system becomes instable. This simple example demonstrates the influence of an electrostatic load on the structural stiffness.

For the FWMAV structure, however, the concept of closely spaced, parallel plates to modify structural properties is not practical due to geometrical discrepancies for relatively large displacements. To enable large rotations or displacements, designs with curved electrodes (i.e., *zipper* actuators) have been reported [36]. An example of a deflecting beam configuration with curved electrodes to which a voltage V is applied, is shown in figure 4. The electric field strength (i.e., $E = V/d$) decreases towards the free tip of the harmonically deflecting, conducting beam. If the beam deflects towards one of the electrodes, the electric field increases on that side while decreasing on the other side. The electrodes are covered by a dielectric layer to prevent short circuit between the conducting beam and the electrodes for large deflections of the beam.

The electrostatic load F_{el} per unit beam length between the beam and one of the electrodes can be given by [36]

$$F_{el}(x_{\mathrm{el}}, V, t) = \frac{\varepsilon_0 b V^2}{2\left[t_d/\varepsilon_r + d(x_{\mathrm{el}}, t)\right]^2} \tag{9}$$

where b represents the width of the electrode and the beam, t_d the thickness of the dielectric layer, ε_0 the vacuum permittivity, ε_r the relative permittivity of the dielectric layer, and $d(x_{\mathrm{el}}, t)$ the distance between

the beam and the electrode at location x_{el} at time t. Modest changes in the shape or curvature of the two electrodes can lead to significant changes of the electrostatic load of (9) [37]. Recently, the working principle of zipper actuators was demonstrated on a walking, printable robot [38].

The use of zipper-based, curved electrodes in FWMAV designs to induce structural softening becomes more attractive for decreasing sizes. Advantages of this method are: 1) the absence of physical contact between the electrodes which increases reliability, and 2) the power consumption is low since the current is theoretically zero. Potential disadvantages are: 1) whenever dust particles in the air stick to the electrodes, the performance of the method will degrade, and 2) the angle of the curved electrodes is chosen in the design phase which limits the deflection since the method is most effective if the gap between the beam and the electrodes becomes small during deflection.

3. Potential response modification

This section studies the potential response modifications resulting from the structural changes as induced by the methods of section 2. More specifically, it studies the potential modifications of the passive pitching motion and, directly related to that, the adjustment of the stroke-averaged lift force due to changes of the elastic hinge properties.

This analysis assumes the flapping wing design to be an elliptical, rigid, thin plate with a uniform mass distribution. The shape of the wing is described by two parameters: $\bar{c}$ and R which are the average chord length and the wing span, respectively [39]. The chord length as a function of the wing parameter r is given by

$$c(r) = \frac{4\bar{c}}{\pi}\sqrt{1 - \frac{r^2}{R^2}}, \tag{10}$$

as shown in figure 5. The elastic hinge in the wing design has width b, length L and thickness t_h and is located at the wing root. The wing
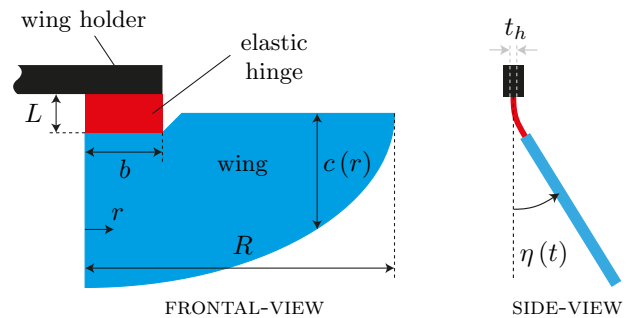

Figure 5. Schematic drawing of elliptical wing design with the elastic hinge connecting the wing holder to the wing. The side-view clarifies the definition of the passive pitching angle $\eta(t)$.

holder connects to the transmission mechanism of the FWMAV design. For completeness, a brief introduction to the passive pitching aerodynamic wing model is given in the following (i.e., the flapping kinematics and the aerodynamic loading). For more details on the aerodynamic model and its validation, the reader is referred to [40].

The spatial motion of the flapping wing can be described using two successive rotational motions, quantified with two Euler angles: 1) the sweeping motion, angle ϕ, and 2) the pitching motion, angle η. The sweeping motion drives the wing to sweep in a horizontal stroke-plane and is assumed to be harmonic (i.e., $\phi(t) = \phi_m \sin(2\pi f t)$, where ϕ_m is the sweeping amplitude, and f is the flapping frequency in Hertz). The pitching motion determines the geometric angle of attack of the flapping wing during the sweeping motion. This work assumes the pitching motion to be achieved passively.

Given the prescribed sweeping motion $\phi(t)$, the rigid wing model involves only one degree of freedom: the pitching angle $\eta(t)$ which is shown schematically in the side-view of figure 5. By applying Euler's second law of motion, the equation of motion that governs $\eta(t)$ can, without going into detail, be given by

$$\tau^{\text{iner}} + \tau^{\text{applied}} = 0 \qquad (11)$$

where τ^{iner} represents the inertial torque and τ^{applied} represents the applied torque acting around the pitching axis which consists of two components: i) the torque from the elastic hinge, and ii) the torque determined by the aerodynamic loads. The transient aerodynamic loads are determined using a quasi-steady aerodynamic model. In this model, the aerodynamic load is decomposed into four components that originate from different sources: 1) from the wing translational velocity due to the sweeping $\phi(t)$, 2) from the wing rotational velocity due to the pitching $\eta(t)$, 3) from the coupling between the wing translational and rotational velocity, and 4) from the added mass effect. The quasi-steady aerodynamic load is also used to determine the stroke-averaged lift force. Solving (11) results in the passive pitching motion $\eta(t)$ as a function of the elastic hinge properties. Consequently, hinge property changes result in passive pitching motion modifications. To induce these active changes, the current passive spring steel elastic hinge is replaced by the methods as presented in section 2.

Motivated by previous work on the FWMAV design of figure 1 [41], we choose the following kinematic and wing design parameters: sweeping amplitude $\phi_m = 1$ rad, flapping frequency $f = 27$ Hz, average chord length $\bar{c} = 18$ mm, wing span $R = 50$ mm. Additionally, we aim for a pitching motion amplitude $\eta_m = 1$ rad. The rotational hinge stiffness values k_{rot} that do result in this pitching amplitude

Table 1. Rotational hinge stiffness, k_{rot}, and corresponding spring steel hinge thickness, t_h, for different values of the wing mass, m_{wing}, to obtain a passive pitching motion amplitude $\eta_m = 1.00$ rad. F_L gives the resulting stroke-averaged lift force.

m_{wing} [mg]	k_{rot} [Nm/rad]	t_h [μm]	F_L [mN]
50	5.4×10^{-4}	24.9	12.12
100	9.5×10^{-4}	30.1	12.33
150	13.4×10^{-4}	33.7	11.98

η_m, for different values of the uniformly distributed wing mass, are shown in table 1 (the wing mass of a hawkmoth, which has similar wing dimensions, is 47 mg [42]). The corresponding thickness t_h of a spring steel hinge (i.e., Young's modulus $E = 210 \times 10^9$ Pa) with length $L = 5$ mm, width $b = 10$ mm, and a rectangular cross-section is determined with 1, $k_{\text{rot}} = EI/L$. table 1 also shows the resulting stroke-averaged lift force, F_L. The variations in F_L are due to differences in the phase difference between the sweeping motion $\phi(t)$ and the pitching motion $\eta(t)$. This phase difference decreases if the wing mass increases since the passive pitching motion is, in that case, more dominated by the inertial loads.

In the following, we apply relatively simple approaches to gain more insight in the influence of the three control methods on the elastic hinge properties and, hence, on the stroke-averaged lift force.

3.1. Control using piezoelectric polymers

The original spring-steel elastic hinge of figure 5 can be replaced by a composite hinge of which an enlarged side-view is shown in figure 6. The hinge is symmetric in thickness direction and consists of a compliant core with facings of polymer piezoelectric material. The core does not contribute significantly to the bending stiffness of the hinge but acts like a spacer to facilitate the functioning of the piezoelectric material. The thickness of the core and the piezoelectric polymer layers is denoted by t_c and t_p, respectively. The thickness of the piezoelectric electrodes is assumed to be negligible.

Figure 6 shows the polarization direction of the piezoelectric polymer (i.e., in the 3-direction) as determined by the material poling. During the pitching motion, the hinge deflects and an electric field is generated in the 3-direction. If the hinge deflects downwards (i.e., positive curvature), the upper and lower piezoelectric layer are, respectively, enlarged and compressed in the 1-direction. Since the deformation in the piezoelectric layers is oppositely, the polarization of the layers is opposite for a proper functioning. The resulting piezoelectric operation configuration is the well-known transverse, in-plane mode for which the
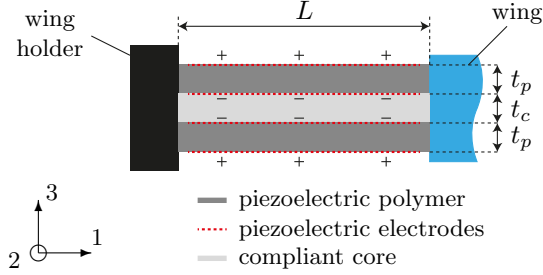
Figure 6. Enlarged side-view schematic of a symmetric hinge with piezoelectric polymer facings and a compliant core. The plus (+) and minus (−) sign indicate the polarization direction. The introduced orthogonal coordinate system agrees with standard piezoelectric conventions.

electromechanical coupling coefficient is determined by $k_{31} = d_{31}/\sqrt{s_{11}^E \varepsilon_3^T}$, see (2).

The electromechanical coupling coefficient and, hence, the property change, increases if the piezoelectric material coupling d_{31} increases for a specific polymer. With a uniaxially oriented polymer, the constant d_{31} can be as high as 22 pC/N for a commercially available piezoelectric PVDF film [43]. For this material the Young's modulus $E_p = 8.3 \times 10^9$ Pa (i.e., $s_{11} = s_{22} = s_{33} = 1/E_p$), and the relative dielectric constant $\varepsilon_r = 10$. Subsequently,

$$k_{31} = \frac{d_{31}}{\sqrt{s_{11}^E \varepsilon_3^T}} = 0.213. \tag{12}$$

The PVDF films are available in three different thicknesses: 28 μm, 52 μm, and 110 μm.

The rotational stiffness of the piezoelectric polymer sandwich of figure 6 is, using (1), given by

$$k_{rot}^{pp} = \frac{b}{12L}\left(E_c t_c^3 + E_p\left((t_c + 2t_p)^3 - t_c^3\right)\right), \tag{13}$$

where $b = 10$ mm is the width of the hinge and E_c represents the Young's modulus of the compliant core which is assumed to be $0.1E_p$ (e.g., a rubber). In the coming sections, sections 3.1.1 and 3.1.2, the dimensions of the active hinge are chosen such that the OC-configuration corresponds to the rotational stiffness values k_{rot} as given in table 1 for the different wing masses (i.e., $k_{rot} = k_{rot}^{OC}$). With a polymer film

Table 2. Steady-state SC passive pitching amplitude, η_m^{SC}, and stroke-averaged lift force, F_L^{SC}, for different values of the wing mass, m_{wing}. The ratio between the SC and OC lift force determines the relative increase.

m_{wing} [mg]	η_m^{SC} [rad]	F_L^{SC} [mN]	F_L^{SC}/F_L^{OC} [-]
50	1.033	12.28	1.013
100	1.045	12.79	1.037
150	1.046	12.55	1.048

thickness $t_p = 28$ μm, the thickness of the core layer t_c is 16.2 μm, 32.2 μm, and 44.1 μm for a wing mass of 50 mg, 100 mg, and 150 mg, respectively. For the other possible film thicknesses (i.e., 52 and 110 μm) the resulting rotational stiffness is larger than the highest required k_{rot} even if $t_c = 0$. Figure 7 shows a schematic zoom-in of the different investigated switch circuits (i.e., OC to SC and OC to RC) as applied to the piezoelectric active hinge.

3.1.1. Lift force change due to an OC to SC switch Switching from OC to SC results in a decrease of the piezoelectric hinge stiffness. For the current piezoelectric configuration, the relation between the SC-Young's modulus and the OC-Young's modulus is (see 3) given by

$$E_p^{SC} = E_p^{OC}\left(1 - k_{31}^2\right), \tag{14}$$

where the electromechanical coupling coefficient k_{31} is given by (12). Subsequently, the ratio between the SC-rotational stiffness k_{rot}^{SC} and the OC-rotational stiffness k_{rot}^{OC} is, with (13), 0.955.

Table 2 shows the steady-state passive pitching amplitude, η_m^{SC}, and the stroke-averaged lift force, F_L^{SC}, if the circuit is switched to SC (i.e., the rotational stiffness becomes k_{rot}^{SC}) for the different wing masses. Additionally, it shows the ratio between the SC lift force, F_L^{SC}, and the OC lift force, F_L^{OC} (see table 1). For all three values of the wing mass, the passive pitching amplitude and the stroke-averaged lift force increase. However, the increase is most significant (especially while considering the lift force) for the wing with the highest mass.

3.1.2. Lift force change due to an OC to RC switch Switching from OC to RC results in a decrease of the piezoelectric hinge stiffness *and* an increase of the damping. The decrease of the stiffness (although moderate compared to switching from OC to SC) results in an increase of the passive pitching angle, as shown by the results of table 2. On the other hand, the increase in damping results, intuitively, in a decrease of the pitching amplitude. Hence, the two structural property changes counteract.

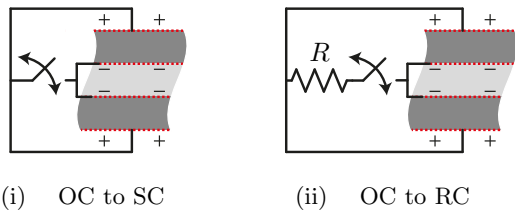(i)   OC to SC   (ii)   OC to RC

Figure 7. Schematic zoom-in of the two utilized switch circuits for the piezoelectric active hinge. OC = open-circuit, SC = short-circuit, and RC = resistive-circuit.

Table 3. Steady-state RC passive pitching amplitude, η_m^{RC}, and stroke-averaged lift force, F_L^{RC}, for different values of the wing mass, m_{wing}. The ratio between the RC and OC lift force determines the relative change.

m_{wing} [mg]	η_m^{RC} [rad]	F_L^{RC} [mN]	$F_L^{\mathrm{RC}}/F_L^{\mathrm{OC}}$ [-]
50	0.990	12.02	0.992
100	0.996	12.32	0.999
150	0.996	12.04	1.005

To study the limit case, we assume the stiffness change due to the switch between OC and RC to be zero. As such, we only study the decrease of the passive pitching amplitude due to the introduced damping. For the current piezoelectric configuration the maximal attainable damping ratio is (see (4)) given by

$$\zeta^{\mathrm{RC}} = \frac{k_{31}^2}{4\left(1 - k_{31}^2\right)} = 0.012, \tag{15}$$

where k_{31} is given by (12). The introduced damping is added to the equation of motion of the passive pitching wing (see (11)) by introducing a damping torque τ^{RC}. This damping torque is assumed to be determined using a linear viscous damper with damping constant $c_{\mathrm{rot}}^{\mathrm{RC}}$ [44]. That is,

$$\tau^{\mathrm{RC}} = c_{\mathrm{rot}}^{\mathrm{RC}} \dot{\eta}, \quad \text{where} \quad c_{\mathrm{rot}}^{\mathrm{RC}} = c_{\mathrm{rot},c} \zeta^{\mathrm{RC}}. \tag{16}$$

In (16), $c_{\mathrm{rot},c}$ represents the critical damping value which is determined by $2\sqrt{k_{\mathrm{rot}} I_\eta}$ where I_η is the wings moment of inertia about the pitching axis.

Table 3 shows the steady-state passive pitching amplitude, η_m^{RC}, and the stroke-averaged lift force, F_L^{RC}, if the circuit is switched to RC (i.e., the rotational stiffness becomes $k_{\mathrm{rot}}^{\mathrm{RC}}$) for the different wing masses. Additionally, it shows the ratio between the RC-lift force, F_L^{RC}, and the OC-lift force, F_L^{OC}. The table indicates that the introduced damping results only in a marginal decrease of the passive pitching amplitude (i.e., $< 1\%$). This damping due to the piezoelectric shunting is small as compared to the aerodynamic damping. The piezoelectric damping introduces, additionally, small changes to the phase difference between the sweeping motion, $\phi(t)$, and the pitching motion, $\eta(t)$ which explains why the stroke-averaged lift force either increases (i.e., $m_{\mathrm{wing}} = 150$ mg) or decreases.

It can be concluded that, in this FWMAV configuration, switching from OC to SC introduces more significant changes to the stroke-averaged lift force as compared to switching from OC to RC. The induced changes would be even more significant if the material dependent electromechanical coupling coefficient k_{31} increases.
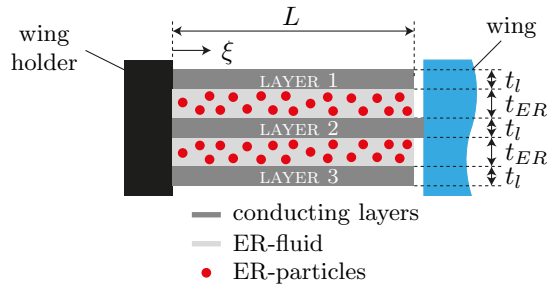

Figure 8. Enlarged side-view schematic of a symmetric hinge with constrained layers of ER-fluid between conducting layers. ξ represents the coordinate along the length of the hinge.

3.2. Control using constrained ER-fluids

The original spring-steel elastic hinge of figure 5 can be replaced by a composite hinge with constrained layers of ER-fluid of which an enlarged side-view is shown in figure 8. The hinge is symmetric in thickness direction and consists of two layers of ER-fluid constrained by conducting layers (e.g., spring steel). We assume that the ER-fluid affects only damping without contributing to the bending stiffness of the hinge. Hence, the rotational stiffness is determined by the three conducting facings only. The thickness of the fluid layers and the conducting layers is denoted by t_{ER} and t_l, respectively. The width and length of the hinge are denoted by b and L, respectively. During the pitching motion $\eta(t)$ the ER-fluid is assumed to remain constrained between the facings using, for example, an encapsulation. It is, additionally, assumed that the thickness of the ER-fluid layers remains constant during the pitching motion.

During the large pitching motion, the hinge deflects and the outer conducting layers (i.e., Layer 1 and 3) will slip with respect to the central conducting layer (i.e., Layer 2). This relative slip results in a shear strain $\gamma(t)$ and, hence, a shear stress in the ER-fluid layers. For an ER-fluid this shear stress can, according to 6, be given as a function of the electric field strength E (unit kV/mm). That is,

$$\tau(E, \xi) = \tau_y(E) + \mu \dot{\gamma}(\xi), \tag{17}$$

where τ_y represents the field dependent yield stress, μ the viscosity (μ is assumed to be independent of E since its variations are marginal compared to the variations of τ_y as a function of E [30]), and $\dot{\gamma}(\xi)$ the shear strain rate which varies over the length of the hinge. This shear stress introduces power dissipation between the layers which can be given by

$$P^{\mathrm{ER}}(E, t) =$$
$$b \int_0^L \tau(E, \xi) \left(v_{12}(\xi, t) + v_{23}(\xi, t)\right) \mathrm{d}\xi \tag{18}$$

where $v_{12}(\xi,t)$ and $v_{23}(\xi,t)$ represent the relative velocity between Layer 1 and 2 and between Layer 2 and 3, respectively. At the wing holder (i.e., $\xi = 0$), this relative velocity will be zero and it will be maximal at $\xi = L$. The introduced damping due to the power dissipation is added to the equation of motion of the passive pitching wing (see (11)) by introducing a damping torque τ^{ER}. That is,

$$\tau^{\mathrm{ER}} = P^{\mathrm{ER}}(E,t)/\dot{\eta}, \tag{19}$$

where $\dot{\eta}$ represents the pitch rate.

To actively control the passive pitching motion $\eta(t)$ and, hence, the stroke-averaged lift force with this composite hinge, the power dissipation due to the ER-fluid layer needs to be changed. By applying a voltage V to Layer 1 and Layer 3 while connecting Layer 2 to ground an electric field E will be induced over the ER-fluid layer which aligns the constituent particles, see figure 9. This alignment results in an increase of the yield stress τ_y (i.e., the first term of 17).

For ER-fluids, the viscosity μ and maximal electric field-induced yield stress τ_y^{max} depend largely on the fluid composition. Additionally, thin layers of ER-fluid, as considered in this example, are not often dealt with in literature. However, to obtain an indication of the applicability of this method in controlling the passive pitching motion $\eta(t)$ we used typical ER-fluid properties reported in literature [22]: viscosity $\mu = 0.2$ Pa·s and the maximal field-induced yield stress $\tau_y^{\mathrm{max}} = 5$ kPa.

The rotational stiffness of the hinge of figure 8 is given by an equation similar to 13. The width of all layers is equal, $b = 10$ mm, and the conducting layers are made of spring steel (i.e., $E_l = 210 \times 10^9$ Pa) with a thickness of $t_l = 5$ μm. The ER-fluid layer itself does not add to the rotational stiffness. The thickness of the ER-fluid layer, t_{ER}, is chosen such that the rotational stiffness of the composite hinge is equal to the rotational stiffness of the reference elastic hinge (i.e., k_{rot}) as given in table 1 for the different wing masses. Subsequently, the thickness of the ER-fluid layer, t_{ER}, is 6.2 μm, 9.9 μm, and 12.8 μm for a wing mass of 50 mg, 100 mg, and 150 mg, respectively. Even in the absence of an electric
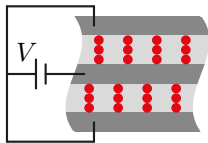

Figure 9. Alignment of particles in the ER-fluid due to the presence of the electric field as induced by applying a voltage V to the conducting layers.

Table 4. Steady-state passive pitching amplitude, η_m^{ER}, and stroke-averaged lift force, F_L^{ER}, for different values of the wing mass, m_{wing}, for a maximal value of the field-induced yield stress, $\tau_y^{max} = 5$ kPa. The ratio between the lift forces determines the relative change.

m_{wing} [mg]	η_m^{ER} [rad]	F_L^{ER} [mN]	F_L^{ER}/F_L [-]
50	0.993	12.04	0.993
100	0.998	12.29	0.997
150	0.998	12.02	1.003

field (i.e., $E = 0$), rotational damping is introduced by the ER-fluid layer due to the second term of 17 (i.e., $\mu\dot{\gamma}(\xi)$). This damping is however marginal as compared to the aerodynamic damping. Hence, for $E = 0$, the passive pitching amplitude η_m and stroke-averaged lift force F_L for the different wing masses are equal to the results of the wing with elastic hinge as shown in table 1.

Table 4 shows the steady-state passive pitching amplitude, η_m^{ER}, and the stroke-averaged lift force, F_L^{ER}, if the power dissipation and, hence, the damping is maximized by using the maximal electric field-induced yield stress, $\tau_y^{\mathrm{max}} = 5$ kPa. Additionally, it shows the ratio between the resulting lift force, F_L^{ER}, and the reference lift force, F_L. The table shows that the changes of the stroke-averaged lift force due to the maximal value of τ_y are less than 1%. Again, the damping torque as induced by the ER-fluid layer is relatively small as compared to the damping torque as induced by the aerodynamic loads.

Above analysis shows only marginal changes of the stroke-averaged lift force using the constrained ER-fluid layer design of figure 8. Possible ways to enhance these changes are: 1) the use of ER-fluids with a higher maximal field-induced yield stress τ_y^{max} (i.e., τ_y^{max} of MR-fluids can be 20× larger [22]), and 2) an approach which combines both a smart structural design *and* an ER-fluid to enable, for example, also control of the shear rate $\dot{\gamma}$.

3.3. Control using electrostatic softening

This method adds two curved electrodes to the wing design to soften the elastic hinge by inducing an electric field, as shown in the zoom-in of figure 10a. By applying a voltage V to the electrodes while shorting the conducting, elastic hinge to ground, an electric field is generated between the electrodes. This effectively softens the elastic hinge. Close to the wing holder, the electric field is highest since the distance between the electrode and the elastic hinge is smallest. The electrodes are covered by a dielectric layer with thickness t_d to prevent a short circuit.

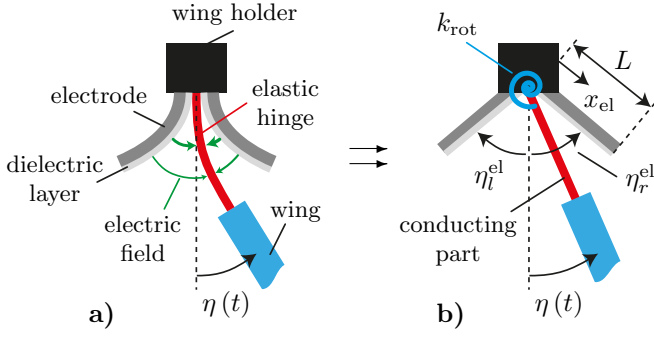The introduced formulation of the rotational

Figure 10. Enlarged side-view schematic of the wing design with electrodes which introduce an electric field to influence the passive pitching motion $\eta(t)$. **a)** electric field between deflecting elastic hinge and curved electrodes to soften the hinge. **b)** approximate model which assumes straight electrodes and an elastic hinge which is replaced by a rotational spring.

stiffness (i.e., $k_{\text{rot}} = EA/L$, see 1), effectively replaces the elastic hinge by a rotational spring. As such, the wing design with elastic hinge is replaced by a rigid pendulum-like pitching wing. To obtain a first estimation of the influence of the electric field on the passive pitching motion $\eta(t)$, the curved electrodes are replaced by straight electrodes with length L. Thus, the model assumes an electrostatic loading over a length L (i.e., the original length of the elastic hinge) between the straight electrodes and a conducting part of the wing as shown in figure 10b. Since the electrostatic loading is directly dependent on the distance between the electrodes and the hinge, the configuration with the curved electrodes experiences a more significant loading during the pitching motion since the hinge is deflecting more closely around the curved electrodes. The model with the straight electrodes, consequently, underestimates the effect. This model, additionally, neglects the complicated peeling off the elastic hinge which (partly) sticks to the electrodes at the maximal pitching amplitude η_m.

Figure 10b shows the fixed angles of the left electrode (i.e., η_l^{el}) and the right electrode (i.e., η_r^{el}). The wing pitches passively between these two electrodes and the electrostatic loading is most significant if the pitching amplitude η_m is closest to either η_l^{el} or η_r^{el}. The non-linear electrostatic loading is added to the equation of motion of the passive pitching wing (see (11)) by introducing two external torques (i.e., τ_l^{el} and τ_r^{el}). With the electrostatic load per unit beam length (see (9)) the torque due to the left electrode can be given by

$$\tau_l^{\text{el}} = \int_0^L \frac{\varepsilon_0 b V^2}{2\left[t_d/\varepsilon_r + d_l(x_{\text{el}}, t)\right]^2} x_{el} \mathrm{d}x_{\text{el}}, \tag{20}$$

where $d_l(x_{\text{el}}, t)$ represents the shortest distance between the left electrode and the pitching wing at a location x_{el} along the electrode at time t. The

Table 5. Steady-state passive pitching amplitude, η_m^{el}, and stroke-averaged lift force, F_L^{el}, for different values of the wing mass, m_{wing}, for an applied voltage of 700 V. The ratio between the lift forces determines the relative increase.

m_{wing} [mg]	η_m^{el} [rad]	F_L^{el} [mN]	F_L^{el}/F_L [-]
50	1.024	12.37	1.021
100	1.012	12.51	1.015
150	1.006	12.10	1.010

torque due to the right electrode is equal to (20) except that the distance $d_l(x_{\text{el}}, t)$ is replaced by $d_r(x_{\text{el}}, t)$, the shortest distance between the right electrode and the wing.

For the different values of the wing mass, the rotational stiffnesses of table 1 are utilized. As such, for $V = 0$ (i.e., no electric field such that $\tau_l^{\text{el}} = \tau_r^{\text{el}} = 0$), the steady-state passive pitching amplitude $\eta_m = 1.00$ rad and the stroke-averaged lift force, F_L, for the different wing masses, is given in table 1. Additionally, we assume the fixed angles of the electrodes $\eta_l^{\text{el}} = \eta_r^{\text{el}} = 1.05$ rad, the relative dielectric permittivity $\varepsilon_r = 3.2$ (e.g., a polymer) and the thickness of the dielectric layer $t_d = 5\ \mu$m.

Table 5 shows the steady-state passive pitching amplitude, η_m^{el}, and the stroke-averaged lift force, F_L^{el}, if a voltage of $V = 700$ V is applied to the electrodes. Additionally, it shows the ratio between the resulting lift force, F_L^{el}, and the reference lift force, F_L. The table shows that the presence of the electric field increases both the pitching amplitude and the stroke-averaged lift force. The changes due to the electrostatic loading decrease if the mass of the wing increases. Whenever the applied voltage V becomes too high, the wing sticks to one of the electrodes and the pitching amplitude becomes equal to the fixed electrode angle, either η_l^{el} or η_r^{el}. The maximal voltage V that can be applied before the wing sticks to the electrode decreases whenever the ratio between the electrostatic torques (i.e., τ_l^{el} and τ_r^{el}) and the inertial torque (i.e., τ^{iner}) increases (i.e., a lightweight wing sticks for a lower applied voltage V compared to a heavier wing).

3.4. Concluding remarks about different methods

This section presented quantitative approaches to obtain a first estimation of the potential response modifications (i.e., lift force changes) resulting from three different methods to change the structural properties of the elastic hinge. For the piezoelectric OC to RC switch and for control using constrained ER-fluids the stroke-averaged lift force changes are found to be less than 1 %. For the piezoelectric OC to SC switch, the stroke-averaged lift force changes up to almost 5 % while electrostatic softening might change

the stroke-averaged lift force up to 2 %. The uniform weight of the wing has a clear influence on the potential lift force changes. Some methods perform better for higher wing masses (i.e., OC to SC switch) and some methods perform better for lower wing masses (i.e., electrostatic softening). To put the obtained stroke-averaged lift force changes into perspective, the maneuverability of a lightweight FWMAV design due to the induced lift force change will be studied in the next section.

4. FWMAV maneuverability due to induced lift force difference

In the absence of disturbances, a perfectly symmetric FWMAV design hovers stationary and stable if the lift production, which is sufficient for the FWMAV to stay aloft, is equally distributed over the flapping wings. However, factors like manufacturing inaccuracies and environmental disturbances result in an instable system. For stable flight, active control is demanded which can be achieved using, for example, stroke-averaged lift force changes. In the previous section, the stroke-averaged lift force change due to three different control methods has been determined. This section studies the influence of these lift-force changes on the maneuverability of the lightweight FWMAV design using analytical models. It does so by determining the required time T_m to perform a 2D horizontal translation over a distance $X_m = 0.5$ m for several stroke-averaged lift force differences (i.e., $1 \%, 2 \%, \ldots, 5 \%$) between opposite wings.

The control maneuver is shown schematically in figure 11. At $t = 0$, the FWMAV hovers stationary at $x = 0$ with a horizontal velocity $v_h = 0$ m/s. At this point, the force in the vertical direction, F_v, is equal to the lift force, F_L, or thrust force as generated by the flapping wings to keep the FWMAV aloft. Due to a proper lift force difference, ΔF_L, between opposite wings, the FWMAV starts to roll through an angle θ

in clockwise direction. This roll results in a force F_h in horizontal direction since F_L remains perpendicular to the wing's stroke-plane. Consequently, the FWMAV accelerates in horizontal direction. To hover stationary again at $x = X_m$ (i.e., $\theta = 0°$ and $v_h = 0$ m/s), the FWMAV needs to roll back (i.e., counterclockwise) to decelerate. Hence, during the maneuver, the wing that produces more lift (i.e., a ΔF_L difference) changes back and forth between opposite wings.

During roll, we assume an active adjustment of F_L such that F_v remains constant (i.e., constant to lift the $0.5cm$ FWMAV mass of 4 gram) during the entire maneuver to prevent any accelerations in vertical direction. F_L is directly related to F_v via the angle θ. We assume a maximal F_L adjustment of 50% using, for example, sweep amplitude changes.

With Euler's second law of motion, the roll acceleration around the FWMAV center of mass (COM) is given by

$$\ddot{\theta} = \frac{\Delta F_L l_L}{I_{\text{FWMAV}}}, \tag{21}$$

where ΔF_L represents the stroke-averaged lift force difference between opposite wings, l_L represents the distance between the COM of the FWMAV and the center of lift (COL) of the wing, and I_{FWMAV} is the moment of inertia of the FWMAV around the COM. For a graphical interpretation of the introduced parameters see figure 12.

This section uses the structural dimensions of the four-wing FWMAV of figure 1 [41]. The length $l_L = r_r + d_{\text{COL}}$ where $r_r = 14$ mm is the radius of the ring structure [41] and d_{COL} is assumed to be $0.6R$ [45]. I_{FWMAV} can be divided in three parts,

$$I_{\text{FWMAV}} = I_w + I_m + I_{a+p}, \tag{22}$$

where I_w, I_m, and I_{a+p} represent the moment of inertia due to the wings, the wing actuation mechanism (i.e., rings and hinges), and the actuators and additional payload (e.g., sensors), respectively. That is:

- Due to symmetry in the design, we assume that I_w is determined by two wings only. Subsequently, $I_w = 2\left(m_{\text{wing}} l_w^2\right)$ where $l_w = r_r + d_w$ represents
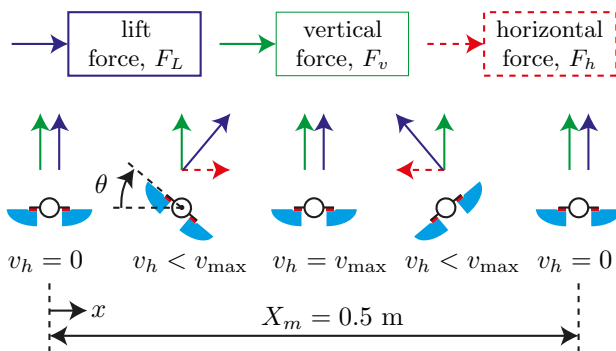

Figure 11. Schematic of a 2D horizontal translation of a FWMAV design due to a lift force difference between opposite wings with the definition of the roll angle θ.
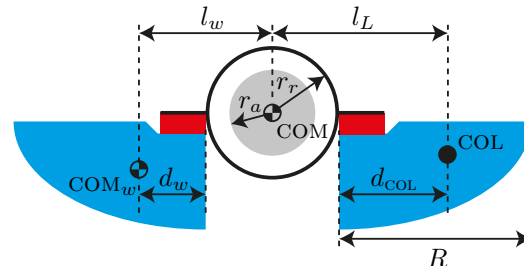

Figure 12. Definition of parameters to determine the moment inertia to roll around the center of mass, COM, of the FWMAV.
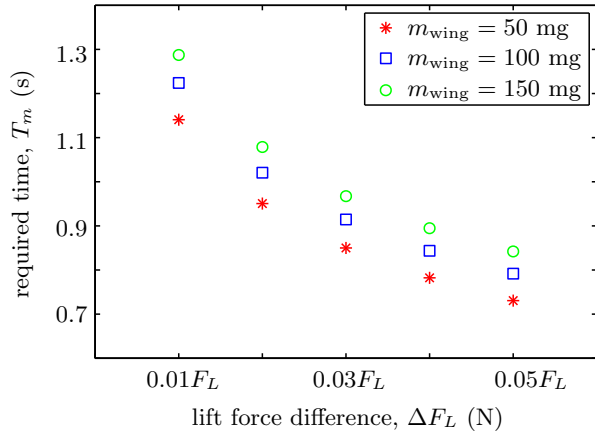
Figure 13. Required time T_m for a controlled horizontal translation X_m for different stroke-averaged lift force differences, ΔF_L, and wing masses, m_{wing}.

the distance between the FWMAV COM and the center of mass of the wing (COM$_w$). Since the mass of the wing is uniformly distributed the wing is represented as a point mass. For the current elliptical wing design $d_w = 0.434R$;

- The mass m_m of the wing actuation mechanism is assumed to be concentrated in the wall of a thin-walled tube with radius r_r. Subsequently, $I_m = m_m r_r^2$ with $m_m = 0.5$ gram [41]; and

- Since the total FWMAV mass is restricted to 4 gram, the total mass of the actuator and payload is restricted to $m_{a+p} = 4 - m_m - 4m_{\text{wing}}$. We assume the mass m_{a+p} to be concentrated in a solid, uniform sphere with radius $r_a = 0.8r_r$ inside the ring structure. This gives $I_{a+p} = 2m_{a+p}r_a^2/5$.

Subsequently, the roll motion $\theta(t)$ can be determined for a lift force difference ΔF_L between opposite wings. Based on the previous section, ΔF_L is chosen to be $0.01F_L$, $0.02F_L$, ..., $0.05F_L$. These ΔF_L are applied to the FWMAV designs with different wing mass values (i.e., 50 mg, 100 mg, and 150 mg). Since X_m is only 0.5 m, the maximal adjustment of F_L during roll, to keep F_v constant, is always below 40%.

The resulting required time T_m to accomplish a controlled, horizontal maneuver of $X_m = 0.5$ m, is shown in figure 13. For a FWMAV with $m_{\text{wing}} = 50$ mg the time T_m decreases by 36% if ΔF_L becomes 5× higher. The required time T_m appears to decrease monotonically towards a minimum value for which an even higher ΔF_L scores minimal effect. The maneuver X_m is about 14% faster for a FWMAV with low-mass wings (i.e., 50 mg) compared to FWMAV for which $m_{\text{wing}} = 150$ mg. Although the mass m_{a+p} is higher for a FWMAV with low-mass wings (i.e., total FWMAV is constant), the total contribution to the moment of inertia around the roll axis is less compared to the design with more heavy wings.

Although this maneuverability study is restricted to roll in a 2D-plane only, it demonstrates the maneuverability of lightweight FWMAV designs. Depending on the situation, small stroke-averaged lift force differences (i.e., only 1%) might be already sufficient to result in the required maneuver speed. Issues with respect to FWMAV stability and environmental disturbances are not discussed in this work.

5. Discussion

This work investigated three methods to induce (local) structural property changes to a vibrating structure to modify its dynamic response. These methods use, respectively, piezoelectric polymers, electrorheological fluids and electrostatic softening. The focus was, primarily, on simple yet insightful ways to determine whether or not a method was able to induce sufficient changes rather than on the exact modeling of these methods.

The achievable structural property changes with piezoelectric polymers do largely depend on the electromechanical coupling factor. For polymers, this factor is significantly lower as compared to piezoelectric ceramics. However, due to the high material deformations within FWMAV designs, only polymers are applicable. Further advances in compliant piezoelectric materials might lead to even more significant structural property changes and applications in structural vibration control.

The damping for the resistively shunted piezoelectric material was relatively low compared to the aerodynamic damping. The maximal achievable damping ratio (i.e., 0.012) was too low to introduce significant response modifications. Higher damping ratio's can be achieved by using well-known resistive-inductive-circuits (i.e., RL-shunt). These circuits, however, require high inductance values in order to function properly which is practically impossible to manufacture within the FWMAV constraints on weight and space. One approach to circumvent this problem is the introduction of electronic circuits (gyrators) to simulate inductance behavior [46].

For the method which uses electrorheological fluids (ERFs), the achievable property change and stroke-averaged lift force modification was negligible. The maximal damping due to the ERF was small compared to the aerodynamic damping. This damping can be increased if the material-dependent maximal field-induced yield stress can be improved with more advanced ERFs. Additionally, a combination between a smart structural design *and* an ERF might improve the response modification. In that case, activation might also change, for example, the shear rate in the

ERF which also influences damping.

The mass of the wing has a large influence on the potential response modification. As such, the control method to implement on the FWMAV might be motivated by the mass of the flapping wing. Piezoelectric methods perform better if the wing mass increases while electrostatic methods perform better if the wing mass decreases. Although, these observations are strongly linked to the studied FWMAV wing, the mass distribution in lightweight, complex structures plays, in general, an important role in the effectiveness of control approaches.

The change of the stroke-averaged lift force is not only determined by the change of the passive pitching amplitude. For example, table 2 shows an increase of the passive pitching amplitude of 3.3% and an increase of the lift force of 1.3% whereas table 5 shows an increase of the pitching amplitude of 2.4% and an increase of the lift force of 2.1%. Hence, the lift force changes are also caused by modifications of, for example, the phase difference between the sweeping motion $\phi(t)$ and the pitching motion $\eta(t)$, and the course or behavior of the passive pitching motion (i.e., its deviation from a harmonic motion). This work solely investigated the change of the stroke-averaged lift force without looking to the required power to obtain the flapping motion.

The compliant elastic hinge in the wing design was replaced by active symmetric composites (i.e., for the piezoelectric and the smart fluid). This resulted in very thin layers of material (i.e., even smaller than $20~\mu m$) which might be difficult to manufacture in real-life practice. Hence, the finally achievable property change in the experimental setup might deviate from the optimal theoretical values as adopted in this work. The manufacturing process and implementability of the different methods is, however, neglected in this work.

A repeatable, reliable and neat production process is, however, necessary for a correct functioning of these methods. Especially the method based on electrostatic softening is very sensitive to variations of the design (i.e., the gap between the electrodes and the conducting layers). For proper FWMAV controllability, manufacturing approaches should be designed to ensure that the control mechanism on each wing has similar characteristics in terms of inducible property changes. Printed circuit board manufacturing techniques on thin film printing [47] might be utilized to produce the control mechanisms in a repeatable, reliable and new way.

6. Conclusions

This work presents a theoretical study on possible methods to induce structural property changes in small and lightweight vibrating structures in order to modify their dynamic response. The methods are based on: piezoelectric polymers, constrained electrorheological fluid layers, and electrostatic softening. The presented description of the individual methods resulted in simple yet insightful ways to determine the potential structural property change.

The study on the maneuverability of the lightweight FWMAV design revealed that stroke-averaged lift force differences between opposite wings of only 1 % could already result in a desired maneuver speed. Methods based on piezoelectric polymers (i.e., switching between open-circuit and short-circuit) or electrostatic softening are, consequently, theoretically feasible to achieve the desired performance. Methods based on piezoelectric polymers with resistive circuits or constrained electrorheological fluid layers are, however, not feasible since the introduced damping due to activation of these methods is relatively small compared to the aerodynamic damping and the resulting lift force modification is smaller than 1 %. The latter two methods might become effective for the control of systems with a relatively low level of damping.

The different methods are applied to the elastic hinge of a FWMAV wing design to modify the passive pitching amplitude and, hence, the stroke-averaged lift force. The resulting problem was complex and highly multi-disciplinary: structural dynamics, flapping wing aerodynamics and electrostatics. Although the methods are applied to this specific example, it clearly demonstrates the complex facets and interdependencies between disciplines that generally appear during the control of lightweight complex structures.

In this work, the three different methods or actuation principles are employed to induce property structural changes. However, in general, piezoelectric materials are applied as actuators or sensors, electrorheological fluids are applied in relatively large scale clutches, and the curved electrode configuration is known as the *zipper* actuator. As such, these methods are not primarily intended to change structural properties. Hence, there is a need for new approaches or actuators that are well-suited to induce significant property changes in a fast and controlled manner within the context of lightweight structures.

The current study is purely theoretical and requires, as a next step, an experimental validation of the different methods to demonstrate their practical applicability. After that, these methods should be integrated within a full-scale FWMAV design to show its ability to control flights.

Acknowledgements

Bibliography

[1] A. Preumont. *Vibration Control of Active Structures: an Introduction*, volume 179. Springer, 2011.

[2] E.S. Leland and P.K. Wright. Resonance tuning of piezoelectric vibration energy scavenging generators using compressive axial preload. *Smart Materials and Structures*, 15(5):1413–1420, 2006.

[3] M.L. Anderson and R.G. Cobb. Toward flapping wing control of micro air vehicles. *Journal of Guidance, Control, and Dynamics*, 35(1):296–308, 2012.

[4] S. Korkmaz. A review of active structural control: challenges for engineering informatics. *Computers and Structures*, 89(23-24):2113–2132, 2011.

[5] M. Géradin and D. Rixen. *Mechanical Vibrations: Theory and Application to Structural Dynamics*. John Wiley & Sons, 3rd edition, 2014.

[6] W.W. Clark. Vibration control with state-switched piezoelectric materials. *Journal of Intelligent Material Systems and Structures*, 11(4):263–271, 2000.

[7] R. Stanway. Smart fluids: current and future developments. *Materials Science and Technology*, 20(8):931–939, 2004.

[8] C. Peters, D. Maurath, W. Schock, F. Mezger, and Y. Manoli. A closed-loop wide-range tunable mechanical resonator for energy harvesting systems. *Journal of Micromechanics and Microengineering*, 19(9), 2009.

[9] M. Sreekumar, T. Nagarajan, M. Singaperumal, M. Zoppi, and R. Molfino. Critical review of current trends in shape memory alloy actuators for intelligent robots. *Industrial Robot*, 34(4):285–294, 2007.

[10] C. T. Bolsman, J. F. L. Goosen, and F. van Keulen. Design overview of a resonant wing actuation mechanism for application in flapping wing mavs. *International Journal of Micro Air Vehicles*, 1(4):263–272, 2009.

[11] L. L. Howell. *Compliant Mechanisms*. Wiley, 2001.

[12] I.K. Kuder, A.F. Arrieta, W.E. Raither, and P. Ermanni. Variable stiffness material and structural concepts for morphing applications. *Progress in Aerospace Sciences*, 63:33–55, 2013.

[13] H. J. Peters, J. F. L. Goosen, and F. van Keulen. An inventory of structural changes to modify the dynamic response of lightweight compliant fwmav designs. In n.a., editor, *Proceedings of International Micro Air Vehicle Conference and Flight Competition (IMAV2015)*, 2015. September 15-18, Aachen, Germany.

[14] H. J. Peters, Q. Wang, J. F. L. Goosen, and F van Keulen. Active control of the passive pitching of a flapping wing with electrostatic clamping. In A. L. Araúo, C. A. Soares, and et al., editors, *Proceedings of the 7th ECCOMAS Thematic Conference on SMART Structures and Materials*, 2015. June 3-6, Ponta Delgada, Azores, Portugal.

[15] S.O.R. Moheimani. A survey of recent innovations in vibration damping and control using shunted piezoelectric transducers. *IEEE Transactions on Control Systems Technology*, 11(4):482–494, 2003.

[16] N.W. Hagood and A. von Flotow. Damping of structural vibrations with piezoelectric materials and passive electrical networks. *Journal of Sound and Vibration*, 146(2):243–268, 1991.

[17] N. Jalili. Vibration control using piezoelectric actuators and sensors. In *Piezoelectric-Based Vibration Control*, pages 129–159. Springer US, 2010.

[18] B. de Marneffe. *Active and Passive Vibration Isolation and Damping via Shunted Transducers*. PhD thesis, Université Libre de Bruxelles, December 2007.

[19] J. De Vicente, D.J. Klingenberg, and R. Hidalgo-Alvarez. Magnetorheological fluids: A review. *Soft Matter*, 7(8):3701–3710, 2011.

[20] W.M. Winslow. Induced fibration of suspensions. *Journal of Applied Physics*, 20(12):1137–1140, 1949.

[21] P.P. Phulé and J.M. Ginder. The materials science of field-responsive fluids. *MRS Bulletin*, 23(8):19–22, 1998.

[22] T. Butz and O. von Stryk. Modelling and simulation of electro- and magnetorheological fluid dampers. *ZAMM Zeitschrift fur Angewandte Mathematik und Mechanik*, 82(1):3–20, 2002.

[23] F. Gandhi and W.A. Bullough. On the phenomenological modeling of electrorheological and magnetorheological fluid preyield behavior. *Journal of Intelligent Material Systems and Structures*, 16(3):237–248, 2005.

[24] N. Mohammadi, M.J. Mahjoob, B. Kaffashi, and S. Malakooti. An experimental evaluation of pre-yield and post-yield rheological models of magnetic field dependent smart materials. *Journal of Mechanical Science and Technology*, 24(9):1829–1837, 2010.

[25] S.O. Oyadiji. Applications of electro-rheological fluids for constrained layer damping treatment of structures. *Journal of Intelligent Material Systems and Structures*, 7(5):541–549, 1996.

[26] A.F. Sprecher, J.D. Carlson, and H. Conrad. Electrorheology at small strains and strain rates of suspensions of silica particles in silicone oil. *Materials Science and Engineering*, 95(C):187–197, 1987.

[27] R. Stanway, J.L. Sproston, and A.K. El-Wahed. Applications of electro-rheological fluids in vibration control: a survey. *Smart Materials and Structures*, 5(4):464–482, 1996.

[28] Y. Choi, A.F. Sprecher, and H. Conrad. Vibration characteristics of a composite beam containing an electrorheological fluid. *Journal of Intelligent Material Systems and Structures*, 1(1):91–104, 1990.

[29] W. S. Yen and P. J. Achorn. A study of the dynamic behavior of an electrorheological fluid. *Journal of Rheology*, 35(7):1375 – 1384, 1991.

[30] Y. Sun and M. Thomas. Control of torsional rotor vibrations using an electrorheological fluid dynamic absorber. *JVC/Journal of Vibration and Control*, 17(8):1253–1264, 2011.

[31] C. Majidi and R.J. Wood. Tunable elastic stiffness with microconfined magnetorheological domains at low magnetic field. *Applied Physics Letters*, 97(16), 2010. art. no. 164104.

[32] M. de Volder, K. Yoshida, S. Yokota, and D. Reynaerts. The use of liquid crystals as electrorheological fluids in microsystems: Model and measurements. *Journal of Micromechanics and Microengineering*, 16(3):612–619, 2006.

[33] H. Tai-Ran. *MEMS and microsystems - design and manufacture*. Mechanical engineering series. McGraw-Hill, 2002. ISBN: 9780072393910.

[34] S.G. Adams, F.M. Bertsch, K.A. Shaw, P.G. Hartwell, F.C. Moon, and N.C. MacDonald. Capacitance based tunable resonators. *Journal of Micromechanics and Microengineering*, 8(1):15–23, 1998.

[35] D. Scheibner, J. Mehner, D. Reuter, T. Gessner, and W. Dötzel. A spectral vibration detection system based on tunable micromechanical resonators. *Sensors and Actuators A: Physical*, 123-124:63–72, 2005.

[36] R. Legtenberg, J. Gilbert, S. D. Senturia, and M. Elwenspoek. Electrostatic curved electrode actuators. *Journal*

of Microelectromechanical Systems, 6(3):257–265, Sep 1997.

[37] M. P. Brenner, J. H. Lang, J. Li, and A. H. Slocum. Optimum design of an electrostatic zipper actuator. In Romanowicz B. Laudon M., editor, *Technical Proceedings of the 2004 NSTI Nanotechnology Conference and Trade Show*, volume 2, pages 371–374, Boston, MA, 2004.

[38] A. S. Chen, H. Zhu, Y. Li, L. Hu, and S. Bergbreiter. A paper-based electrostatic zipper actuator for printable robots. In *Robotics and Automation (ICRA), 2014 IEEE International Conference on*, pages 5038–5043. IEEE, 2014.

[39] T. Weis Fogh. Quick estimates of flight fitness in hovering animals, including novel mechanisms for lift production. *Journal of Experimental Biology*, 59(1):169–230, 1973.

[40] Q. Wang, J. F. L. Goosen, and F. van Keulen. Study of design parameters of flapping-wings. In *IMAV 2014: International Micro Air Vehicle Conference and Competition 2014*, 2014. August 12-15, Delft, The Netherlands.

[41] C. T. Bolsman. *Flapping wing actuation using resonant compliant mechanisms An insect-inspired design*. PhD thesis, Delft University of Technology, October 2010.

[42] G.J. Berman and Z.J. Wang. Energy-minimizing kinematics in hovering insect flight. *Journal of Fluid Mechanics*, 582:153–168, 2007.

[43] Precision Acoustics, October 2015. acoustics.co.uk/wp-content/uploads/2013/12/Properties-of-poled-PVDF.pdf.

[44] S.S. Rao. *Mechanical Vibrations*. Pearson Education Centre, 4th edition, 2004.

[45] L. Zhao, Q. Huang, X. Deng, and S. P. Sane. Aerodynamic effects of flexibility in flapping wings. *Journal of the Royal Society Interface*, 7:44, 2010.

[46] A. Antoniou. Realisation of gyrators using operational amplifiers, and their use in rc-active-networks synthesis. In *Proceedings of the Institution of Electrical Engineers*, volume 116, pages 1838–1850, 1969.

[47] P.S. Sreetharan, J.P. Whitney, M.D. Strauss, and R.J. Wood. Monolithic fabrication of millimeter-scale machines. *Journal of Micromechanics and Microengineering*, 22(5), 2012. 055027.